Supporting Information for

Structural Damping Enables Broadband Viscoelastic Low-

Frequency Sound Absorption

Yanlin Zhang^{a,b}, Junyin Li^{b,c}, Qiongying Wu^d, Marco Amabili^b, Diego Misseroni^e, and Hanqing

Jiang^{b,c,f*}

^aSchool of Materials Science and Engineering, Zhejiang University, Hangzhou 310027, China

^bSchool of Engineering, Westlake University, Hangzhou, Zhejiang 310030, China

^cWestlake Institute for Advanced Study, Hangzhou, Zhejiang 310024, China

^dZhejiang Sanlux Rubber Co. Ltd., Shaoxing, Zhejiang 312031, China

^eUniversity of Trento, 38123 Trento, Italy

^fResearch Center for Industries of the Future, Westlake University, Hangzhou, Zhejiang 310030,

China

*Email: <u>hanqing.jiang@westlake.edu.cn</u>

This PDF file includes:

Supporting text

Figs. S1 to S21

Tables S1 to S2

SI References

1

Supporting Text

1. Calculation of sound absorption coefficient under clamped-free boundary conditions

The geometric parameters used in the calculation are illustrated in Fig. S1.

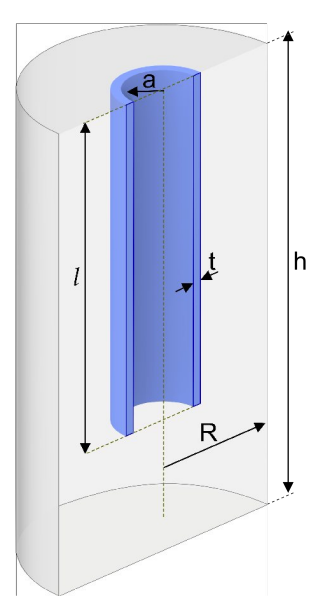


Fig. S1. Cross-sectional schematic of FN-Helmholtz resonator used in the theoretical model. Compared to the configuration in Fig. 2A, the outer shell thickness is omitted, with only the cavity boundary dimensions are considered. The cavity has a height h and radius R. The cylindrical shell has a radius a, thickness t, and length l. The shell material characterized by a Young's modulus E, Poisson's ratio V, density P_S , and loss factor η .

Acoustic impedance of the air column within the neck

The acoustic impedance of the air column within the neck is derived following Crandall theory (1) under the wide-tube approximation. For clarity, we outline the key derivation steps below.

Given that the neck radius a is much larger than the viscous boundary layer thickness $(d_v = \sqrt{\frac{2\mu}{\rho_0 \omega}})$

(2), where μ is the dynamic viscosity, ρ_0 is the air density, ω is the angular velocity), the air column is modeled as a wide tube. The flow behavior in this case is illustrated in **Fig. S2**. During longitudinal acoustic oscillations along the tube axis, viscous effects cause velocity gradients, with the highest velocity at the center of air column and zero velocity at the tube walls. These viscous effects are confined to a thin boundary layer near the wall, while the central "fluid core" exhibits

nearly uniform axial velocity. The motion of this core is hindered by the interaction includes effects of added inertia and resistance. Based on these assumptions, a theoretical model for the fluid motion of the air column in the neck was developed.

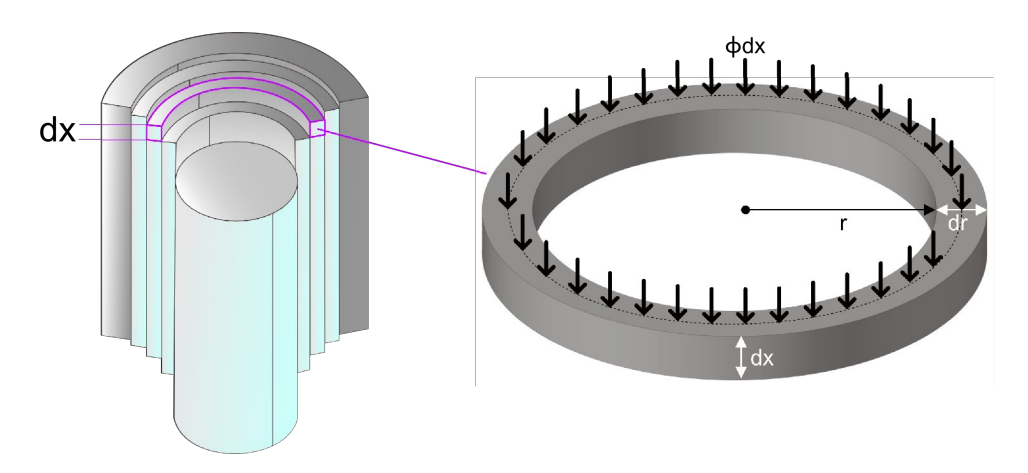


Fig. S2. Schematic illustrating lamellar motion of air in a moderately large tube (left) and the driving force acting on an infinitesimal annular air element (right).

Consider an infinitesimal annular fluid element $2\pi r dr dx$ within the neck (**Fig. S2**, right). The axial driving force per unit area acting on the fluid ring is $\phi \cdot dx$, where ϕ represents the negative pressure gradient parallel to the tube axis ($\phi = -\frac{\partial p}{\partial x}$, p is the air pressure). The total driving force on the annular ring of fluid element is $\phi dx \cdot 2\pi r dr$. This force is opposed by two components:

- 1. Inertial (reactance) force $\rho_0 \cdot 2\pi r dr dx \cdot j\omega \dot{\xi}$ due to fluid acceleration, where $\dot{\xi}$ is the fluid velocity (time derivative of the fluid displacement ξ) along the x-direction.
- 2. The net frictional force $\frac{\partial}{\partial r} \left(-2\pi r dx \cdot \mu \frac{\partial \dot{\xi}}{\partial r} \right) dr$ acting on the annulus. This term is derived from the frictional force on the inner surface of the ring, $-2\pi r dx \cdot \mu \frac{\partial \dot{\xi}}{\partial r}$, the negative sign accounts for the velocity gradient decreasing with increasing radius r. The net force is obtained by evaluating the radial gradient of this shear stress across the thickness dr.

Force equilibrium yields the governing equation:

$$\rho_0 \cdot 2\pi r dr dx \cdot j\omega \dot{\xi} + \frac{\partial}{\partial r} \left(-2\pi r dx \cdot \mu \frac{\partial \dot{\xi}}{\partial r} \right) dr = \phi \cdot 2\pi r dr \cdot dx$$
 [1]

Simplification of this equation yields:

$$\left[j\omega\rho_0 - \frac{\mu}{r} \frac{\partial}{\partial r} \left(r \frac{\partial}{\partial r} \right) \right] \dot{\xi} = \phi$$
[2]

in which only $\dot{\xi}$ is a function of r. It may be written as:

$$\left[\frac{\partial^2}{\partial r^2} + \frac{1}{r}\frac{\partial}{\partial r} + k_v^2\right]\dot{\xi} = -\frac{\phi}{\mu}$$
 [3]

where $k_v = \sqrt{\frac{-j\omega\rho_0}{\mu}}$ represents the viscous wave number.

The solution to this equation is:

$$\dot{\xi} = -\frac{\phi}{\mu k_v^2} + AJ_0(k_v r) \tag{4}$$

here J_0 is the zeroth order Bessel function of the first kind.

To ensure finite velocity at r = 0, and vanishing velocity at the boundary r = a, we determine the constant A. This yields:

$$\dot{\xi}(r) = -\frac{\phi}{\mu k_{v}^{2}} \left[1 - \frac{J_{0}(k_{v}r)}{J_{0}(k_{v}a)} \right]$$
 [5]

Integrating $\dot{\xi}(r)$ over the section (i.e., the circular area with radius a), gives the average velocity:

$$\bar{\dot{\xi}} = \frac{1}{\pi a^2} \int_0^a \dot{\xi} 2\pi r dr = -\frac{\phi}{\mu k_v^2} \frac{2}{a^2} \int_0^a \left[1 - \frac{J_0(k_v r)}{J_0(k_v a)} \right] r dr$$
 [6]

that is:

$$\bar{\dot{\xi}} = -\frac{\phi}{\mu k_{\nu}^{2}} \left[1 - \frac{2}{k_{\nu} a} \frac{J_{1}(k_{\nu} a)}{J_{0}(k_{\nu} a)} \right]$$
 [7]

here J_1 denotes the first-order Bessel functions of the first kind.

The specific acoustic impedance of the air column is defined as the ratio of the pressure drop $\Delta p = \int_0^l \phi dx = \phi l \text{ (over length } l \text{) to the average velocity } \overline{\xi} \text{, that is:}$

$$Z_{l} = \frac{\phi l}{\overline{\xi}} = -\frac{\mu k_{v}^{2} l}{1 - \frac{2}{k_{v} a} \frac{J_{1}(k_{v} a)}{J_{0}(k_{v} a)}}$$
[8]

This impedance incorporates both inertial reactance (imaginary part) and viscous resistance (real part) within the air column.

Additional contributions to the total impedance arise from tube ends. As described by Ingard's theory (3):

1. Viscous losses at both ends contribute a resistance term:

$$R_e = 2\sqrt{2\mu\omega\rho_0}$$
 [9]

2. End radiation introduces a mass reactance term:

$$X_e = j\omega \rho_0 \delta \tag{10}$$

where the effective end correction length δ is given by $\delta = 0.85a \left(2 - 1.25 \frac{a}{R} \right)$.

Combining these with the internal impedance Z_l gives the total specific acoustic impedance:

$$Z_{total} = \frac{-\mu k_{v}^{2} l}{1 - \frac{2}{k_{o}a} \frac{J_{1}(k_{v}a)}{J_{0}(k_{o}a)}} + 2\sqrt{2\mu\omega\rho_{0}} + j\omega\rho_{0}\delta$$
 [11]

Finally, normalizing to the system-level acoustic impedance (pressure per volume velocity) by dividing by the cross-sectional area $S_a = \pi a^2$ yields:

$$Z_{a} = \frac{1}{\pi a^{2}} \left[\frac{-\mu k_{v}^{2} l}{1 - \frac{2}{k_{v} a} \frac{J_{1}(k_{v} a)}{J_{0}(k_{v} a)}} + 2\sqrt{2\mu\omega\rho_{0}} + j\omega\rho_{0} \delta \right]$$
[12]

This integrated expression, synthesizing Crandall's internal flow theory and Ingard's end effects, fully characterizes the acoustic impedance of the neck's oscillatory air column.

Mechanical Impedance of the Cylindrical Shell

The governing equation for cylindrical shell vibration under axisymmetric loading is expressed as (4):

$$D\frac{d^4w}{dx^4} + \frac{Et}{h^2}w = p \tag{13}$$

where p is the distributed inner pressure, w is the radial displacement, x is the axial coordinate, b is the middle-surface radius of the cylindrical shell, and D is the flexural rigidity of the shell.

The middle-surface radius b of the cylindrical shell is given by:

$$b = a + \frac{t}{2} \tag{14}$$

The flexural rigidity of the shell D is defined as:

$$D = \frac{Et^3}{12(1-v^2)}$$
 [15]

Define

$$\beta^4 = \frac{Et}{4a^2D} = \frac{3(1-v^2)}{a^2t^2}$$
 [16]

Substituting into Equation (13), the normalized form becomes:

$$\frac{d^2w}{dx^4} + 4\beta^4 w = \frac{p}{D} \tag{17}$$

For the case of constant pressure p, the general solution of the normalized equation is given by (4):

$$w(x) = \frac{pb^2}{Et} + C_1 \sin(\beta x) \sinh(\beta x) + C_2 \sin(\beta x) \cosh(\beta x) + C_3 \cos(\beta x) \sinh(\beta x)$$

$$+ C_4 \cos(\beta x) \cosh(\beta x)$$
[18]

For a clamped-free cylindrical shell, the boundary conditions are:

At the clamped end (x = 0):

$$w(x,0) = 0, \quad w'(x,0) = 0$$
 [19]

At the free end (x = l):

$$w''(x,l) = 0, \quad w'''(x,l) = 0$$
 [20]

The particular solution satisfying these boundary conditions is:

$$w(x) = \frac{pb^2q(x)}{Et}$$
 [21]

where q(x) is the spatial modulation function:

$$q(x) = 1 + \frac{\left[\sinh^{2}(\beta l) + \sin^{2}(\beta l)\right] \sin(\beta x) \sinh(\beta x)}{\cosh^{2}(\beta l) + \cos^{2}(\beta l)}$$

$$-\frac{\left[\cosh(\beta l) \sinh(\beta l) + \cos(\beta l) \sin(\beta l)\right] \left[\sin(\beta x) \cosh(\beta x) - \cos(\beta x) \sinh(\beta x)\right]}{\cosh^{2}(\beta l) + \cos^{2}(\beta l)}$$

$$-\cos(\beta x) \cosh(\beta x)$$
[22]

Discretized Impedance Model

As shown in **Fig. S3**, the cylindrical shell and the enclosed air column are discretized into n micro-segments of equal length $\frac{l}{n}$ along the axial direction. For each segment i^{th} (i=1,2,...,n), the acoustic impedance of the air column, $Z_a(x_i)$, and the equivalent acoustic impedance of the flexible shell, $Z_b(x_i)$, are connected in parallel, where $x_i = \frac{i}{n}l$ represents the position of the i^{th} segment along the shell axis. Detailed derivations of these impedance components under

clamped-free boundary condition are provided below.

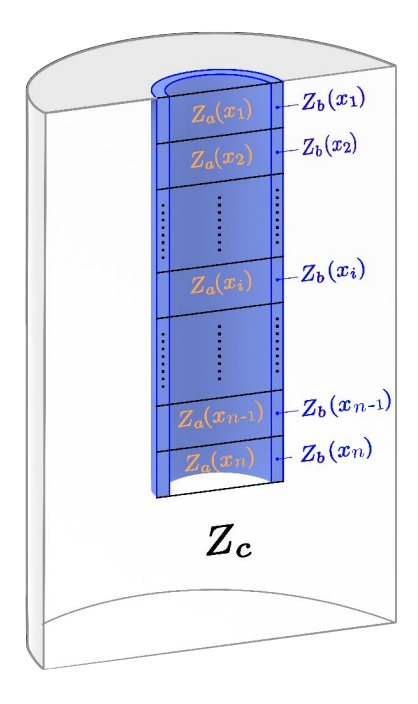


Fig. S3. Cross-sectional schematic of the cylindrical shell and enclosed air column discretized into *n* micro segments of equal length.

The pressure at the position x_i is expressed as:

$$p(x_i) = \frac{F(x_i)}{S(x_i)}$$
 [23]

where $F(x_i)$ and $S(x_i)$ represent the acting force and the lateral surface area of the cylindrical shell segment at position x_i , respectively.

The lateral surface area of the segment at x_i is constant and given by:

$$S(x_i) = \frac{2\pi bl}{n}$$
 [24]

in which $2\pi bl$ is the mid-surface area of the cylindrical shell.

The local equivalent stiffness of the cylindrical shell at position x_i , is defined as:

$$K_m(x_i) = \frac{F(x_i)}{w(x_i)}$$
 [25]

where $w(x_i)$ is the radial displacement at position x_i , given by:

$$w(x_i) = \frac{p(x_i)b^2q(x)}{Et}$$
 [26]

Combining Equations (23) to (26), the local equivalent stiffness is obtained as:

$$K_{m}(x_{i}) = \frac{2\pi l E t}{n b q(x_{i})}$$
 [27]

Poisson effect

When the cylindrical shell undergoes dynamic vibration, neighboring segments experience axial inertial constraints, causing the shell deformation mode to approximate a plane strain state ($\varepsilon_x \approx 0$).

This state reflects stiffness enhancement due to the Poisson effect, and thus, the Young's modulus should be adjusted to an equivalent modulus:

$$E^* = \frac{E}{1 - \nu^2}$$
 [28]

The applicability of this equivalent modulus depends on the excitation frequency:

- 1. At high frequency ($\omega \gg 0$): inertial constraints are significant, and the plane strain assumption holds, so the equivalent modulus $E^* \approx \frac{E}{1-\nu^2}$ is appropriate.
- 2. At low frequency quasi-static ($\omega \to 0$): constraints are negligible, reducing to plane stress state ($\sigma_x \approx 0$), so the equivalent modulus $E^* \approx E$ is appropriate.

Considering the plane strain correction, the local equivalent stiffness is updated to:

$$K_{m}(x_{i}) = \frac{2\pi l E^{*}t}{nbq(x_{i})} = \frac{2\pi l Et}{nb(1-v^{2})q(x_{i})}$$
 [29]

The local mechanical resistance at position x_i is given by:

$$R_m(x_i) = \frac{\eta K_m(x_i)}{\omega}$$
 [30]

The local mass at position x_i is constant and given by:

$$M_m(x_i) = \frac{2\rho_s \pi btl}{n}$$
 [31]

Thus, the local mechanical impedance at position x_i is:

$$Z_{m}(x_{i}) = R_{m}(x_{i}) + j\left(\omega M_{m}(x_{i}) - \frac{K_{m}(x_{i})}{\omega}\right)$$
 [32]

The mechanical-acoustic impedance conversion follows (5):

$$Z_b(x_i) = \frac{Z_m(x_i)}{S(x_i)^2}$$
 [33]

here $Z_b(x_i)$ represents the equivalent acoustic impedance of the flexible cylindrical shell for each segment.

Similarly, the acoustic impedance of the air column for each segment is:

$$Z_a(x_i) = \frac{Z_a}{n} \tag{34}$$

Iterative Calculation of Coupled Acoustic Impedance

The total equivalent impedance Z_e of the system is calculated recursively using the equivalent circuit diagram (Fig. S4).

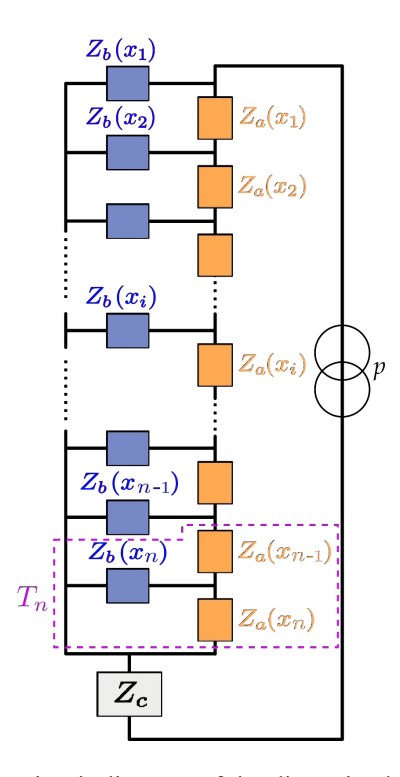


Fig. S4. Equivalent circuit diagram of the discretized impedance model.

Starting from the n^{th} segment, the equivalent impedance, T_n , is computed as the parallel combination of $Z_a(x_n)$ and $Z_b(x_n)$, followed by a series connection with $Z_a(x_{n-1})$:

$$T_{n} = \frac{Z_{a}(x_{n})Z_{b}(x_{n})}{Z_{a}(x_{n}) + Z_{b}(x_{n})} + Z_{a}(x_{n-1})$$
[35]

For the preceding segments, the recursive relationship is expressed as:

$$T_{i-1} = \frac{T_i Z_b(x_{i-1})}{T_i + Z_b(x_{i-1})} + Z_a(x_{i-2}), \quad (i = n, n-1, ..., 3)$$
 [36]

This iterative process continues until the first segment is reached, at which point the coupling impedance between the air column and the shell is fully determined:

$$T_{1} = \frac{T_{2}Z_{b}(x_{1})}{T_{2} + Z_{b}(x_{1})}$$
[37]

where T_1 represents the equivalent impedance of the coupled air column-shell system.

Acoustic Reactance of the Cavity

The system includes the acoustic reactance of the cavity, expressed as (5):

$$Z_c = -j \frac{\rho_0 c_0^2}{\varrho V}$$
 [38]

where the cavity volume V is given by:

$$V = \pi R^2 h - \pi (a+t)^2 l$$
 [39]

Total Acoustic Impedance and Sound Absorption

Finally, the total acoustic impedance of the system is expressed as:

$$Z_e = T_1 + Z_c ag{40}$$

The sound absorption coefficient is calculated as (2):

$$\alpha = 1 - \left| \frac{Z_e S - \rho_0 c_0}{Z_e S + \rho_0 c_0} \right|^2$$
 [41]

where S is the cross-sectional area of the impedance tube ($S = \frac{\pi d^2}{4}$, d being the inner diameter of the tube), and $\rho_0 c_0$ is the characteristic impedance of air. This formula can also be conveniently rewritten in terms of the normalized acoustic resistance $x_s = \text{Re}\left(\frac{Z_e S}{\rho_0 c_0}\right)$ and

normalized acoustic reactance $y_s = \text{Im}\left(\frac{Z_e S}{\rho_0 c_0}\right)$ as (5):

$$\alpha = \frac{4x_s}{(1+x_s)^2 + y_s^2}$$
 [42]

It follows that when Z_e satisfies $Z_eS = \rho_0c_0$ (i.e., $x_s = 1$ and $y_s = 0$), the sound absorption coefficient reaches its maximum value, $\alpha = 1$.

2. Closed analytical form when assuming free boundary conditions at both ends

For a cylindrical shell with free boundary conditions at both ends, the spatial modulation function (Eq. 22) becomes $q(x_i)=1$. The equivalent stiffness $K_m(x_i)$, mechanical resistance $R_m(x_i)$, and mass $M_m(x_i)$ for each segment (Eqs. 29-31) simplify to position-independent constants:

$$\begin{cases} K_{m}(x_{i}) = \frac{2\pi lEt}{nb(1-v^{2})} \\ R_{m}(x_{i}) = \frac{\eta K_{m}(x_{i})}{\omega} \\ M_{m}(x_{i}) = \frac{2\rho_{s}\pi btl}{n} \end{cases}$$
[43]

Substituting Equation (43) into Equations (32) and (33), yields:

$$Z_{b}(x_{i}) = \frac{nEt}{2\pi l\omega b^{3}(1-v^{2})} \left[\eta + j \left(\frac{\omega^{2} \rho_{s} b^{2}(1-v^{2})}{E} - 1 \right) \right]$$
 [44]

Define the equivalent acoustic impedance Z_b for the entire cylindrical shell as:

$$Z_{b} = \frac{Et}{2\pi l\omega b^{3}(1-v^{2})} \left[\eta + j \left(\frac{\omega^{2} \rho_{s} b^{2}(1-v^{2})}{E} - 1 \right) \right]$$
 [45]

Thus, the equivalent acoustic impedance for each segment becomes:

$$Z_b(x_i) = nZ_b ag{46}$$

The acoustic impedance of air in the neck (Eq. 12) can be rewritten as:

$$Z_{a} = \frac{1}{\pi a^{2}} \left[\frac{-\mu k_{v}^{2} l}{1 - \frac{2}{k_{v} a} \frac{J_{1}(k_{v} a)}{J_{0}(k_{v} a)}} + 2\sqrt{2\mu\omega\rho_{0}} + j\omega\rho_{0} \delta \right]$$
 [47]

The acoustic impedance for each segment (Eq. 34) can be re-expressed as:

$$Z_a(x_i) = \frac{Z_a}{n} \tag{48}$$

Infinite Ladder Network Model

The system is modeled as an infinite ladder network (Fig. S5).

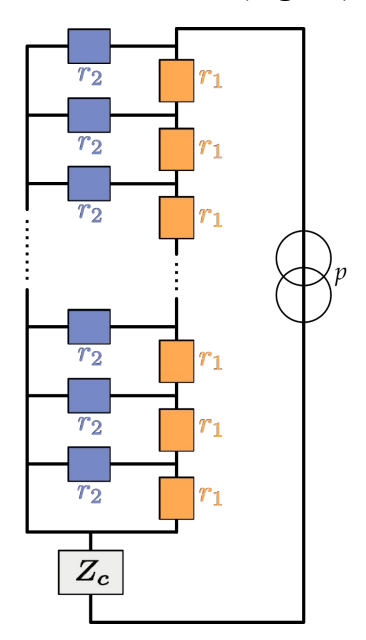


Fig. S5. Infinite ladder network model under free boundary conditions at both ends.

The total impedance is calculated using the following recurrence relation:

$$Z_1 = \frac{r_1 r_2}{r_1 + r_2} + r_1 \tag{49}$$

.

$$Z_{i} = \frac{Z_{i-1}r_{2}}{Z_{i-1} + r_{2}} + r_{1}, \quad (i = 2, 3, ..., n)$$
 [50]

where the parameters are:

$$\begin{cases}
r_1 = Z_a(x_i) = \frac{Z_a}{n} \\
r_2 = Z_b(x_i) = nZ_b
\end{cases}$$
[51]

To facilitate analysis, Equation (50) is reformulated into a standard fractional recurrence form (6):

$$Z_{i} = \frac{r_{1}r_{2} + (r_{1} + r_{2})Z_{i-1}}{r_{2} + Z_{i-1}}$$
 [52]

The objective is to determine the limiting value of Z_n as $n \to \infty$. Since the coefficients r_1 , r_2 are functions of n, we first seek a closed-form expression for Z_i in terms of r_1 and r_2 before evaluating the limit. The solution to the recurrence relation is expressed as a linear fractional transformation:

$$\frac{Z_n - m_1}{Z_n - m_2} = \gamma^{n-1} \frac{Z_1 - m_1}{Z_1 - m_2}$$
 [53]

where the fixed point m_1 , m_2 and attenuation factor γ satisfies:

$$m = \frac{r_1 r_2 + (r_1 + r_2)m}{r_2 + m}$$
 [54]

$$\gamma = \frac{r_1 + r_2 - m_1}{r_1 + r_2 - m_2} \tag{55}$$

Solving quadratic Equation (54) yields two roots:

$$\begin{cases}
 m_1 = \frac{r_1}{2} + \sqrt{\frac{r_1^2}{4} + r_1 r_2} \\
 m_2 = \frac{r_1}{2} - \sqrt{\frac{r_1^2}{4} + r_1 r_2}
\end{cases}$$
[56]

Substituting Equation (51) into the above yields:

$$\begin{cases}
 m_1 = \frac{Z_a}{2n} + \sqrt{\frac{Z_a^2}{4n^2} + Z_a Z_b} \\
 m_2 = \frac{Z_a}{2n} - \sqrt{\frac{Z_a^2}{4n^2} + Z_a Z_b}
\end{cases}$$
[57]

Then attenuation factor γ becomes:

$$\gamma = 1 - \frac{2}{n} \sqrt{\frac{Z_a}{Z_b}} + O\left(\frac{1}{n^2}\right)$$
 [58]

As $n \to \infty$, neglecting infinitesimally small terms, the asymptotic behavior is:

$$\begin{cases} \lim_{n \to \infty} m_1 = \sqrt{Z_a Z_b} \\ \lim_{n \to \infty} m_2 = -\sqrt{Z_a Z_b} \\ \lim_{n \to \infty} \gamma^{n-1} = e^{-2\sqrt{Z_a} \over Z_b} \end{cases}$$
 [59]

Substituting these into Equation (53) gives:

$$\lim_{n \to \infty} Z_n = \frac{1 - e^{-2\sqrt{\frac{Z_a}{Z_b}}}}{1 + e^{-2\sqrt{\frac{Z_a}{Z_b}}}} \sqrt{Z_a Z_b}$$
 [60]

Using the identity $\tanh x = \frac{1 - e^{-2x}}{1 + e^{-2x}}$, the total impedance simplifies to:

$$\lim_{n \to \infty} Z_n = \sqrt{Z_a Z_b} \tanh \sqrt{\frac{Z_a}{Z_b}}$$
 [61]

3. Comparison of Theoretical Models

We compare the absorption predictions from the full-recursive model and the closed-form model for shell lengths of l = 35 mm (Fig. S6A) and l = 55 mm (Fig. S6B). All other geometrical parameters and material properties are held constant (identical to those in Fig. S20). The differences between the full-recursive model (clamped-free) and the closed-form analytical model (free-free) are minor (Fig. S6A), indicating that the closed-form approach still captures the main behavior despite the boundary condition variation. Moreover, this discrepancy diminishes with increasing shell length (l = 55 mm, Fig. S6B), as the influence of end constraints becomes less significant relative to the overall behavior of the shell.

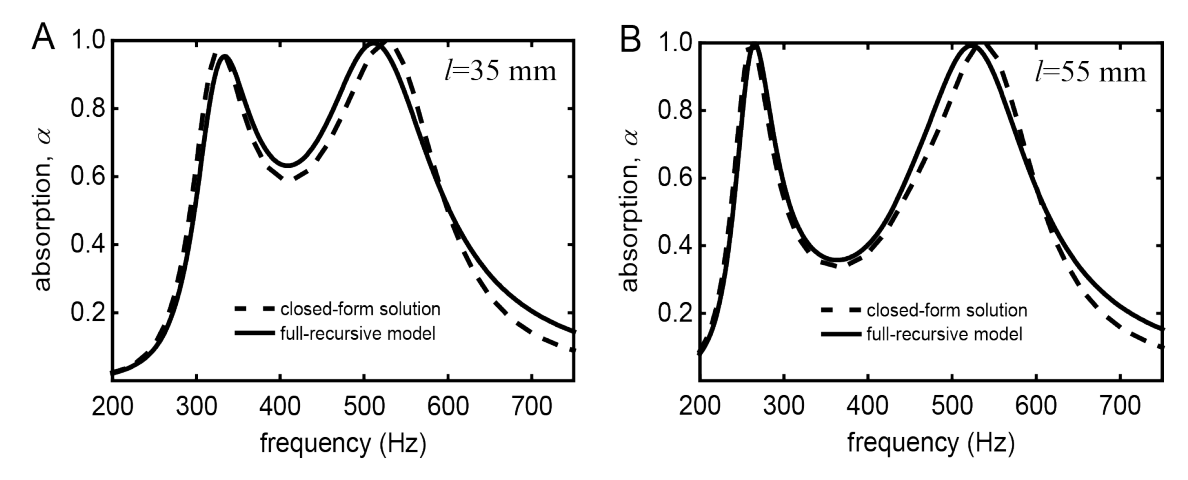


Figure S6. Comparison of absorption predictions based on the closed-form analytical model (free-free boundaries) and full-recursive model (clamped-free boundaries) for shell lengths of **(A)** l = 35 mm and **(B)** l = 55 mm. All other geometrical parameters and material properties are held constant (a = 4 mm, t = 1 mm, R = 13.9 mm, h = 48.8 mm, E = 148.5 kPa, v = 0.49, $\rho_s = 1,070$ kg/m³, $\eta = 0.2$).

4. Viscoelastic Characterization of Silicone Rubber

To characterize the viscoelastic properties (storage modulus E, and loss factor η) of silicone rubber (Ecoflex-30) used in the FN-Helmholtz resonator, we investigated multiple experimental methods: dynamic mechanical analysis (DMA) in compression mode, time-temperature superposition (TTS) for high-frequency extrapolation, and the cantilever beam resonance method per ASTM E756-05. We compared the results obtained from these testing methods.

Dynamic Mechanical Analysis (DMA)

DMA was performed using a TA Instruments DMA 850 analyzer in compression mode (setup shown in **Fig. S7A**). Square samples (dimensions: $18 \times 18 \times 6$ mm³, **Fig. S7B**) were tested under frequency sweeps from 1 Hz to 181 Hz at 10 Hz intervals, with a strain amplitude of 0.5% and at a constant temperature of 25°C. The sample dimensions were optimized to minimize data fluctuations and instability at higher frequencies.

Time-Temperature Superposition (TTS)

To extend the DMA data beyond 181 Hz, we conducted additional experiments using the TTS principle (7). The sample was tested over a temperature range from 25°C to -30°C in 5°C intervals. At each temperature, frequency sweeps were performed at discrete points: 1 Hz, 10 Hz, 30 Hz, 50 Hz, 70 Hz, 90 Hz, 110 Hz, 130 Hz, 150 Hz, and 170 Hz. The raw data for storage modulus and loss factor versus frequency at different temperatures are shown in **Fig. S7C and S7D**, respectively. The results show that both parameters increase slightly as the temperature decreases.

Then, the curves can be horizontally shifted to a reference temperature (25°C) according to the Williams–Landel–Ferry (WLF) equation (8):

$$\log a_{T} = -\frac{C_{1}(T - T_{ref})}{C_{2} + (T - T_{ref})}$$
 [62]

where a_T is the shift factor, T_{ref} is the reference temperature, and empirical constants C_1 and C_2 were fitted from the data.

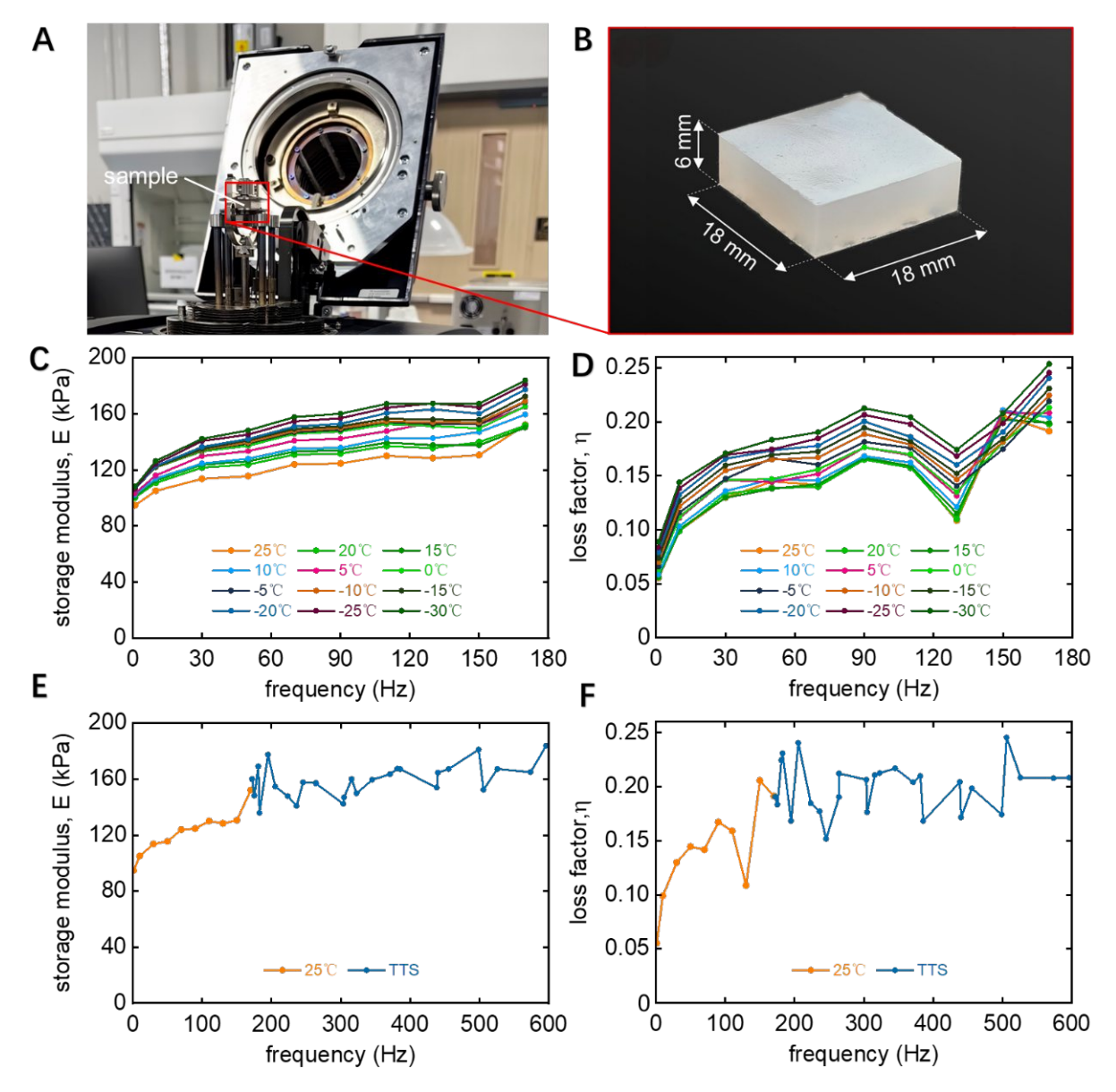


Fig. S7. Dynamic Mechanical Analysis (DMA) Setup and Viscoelastic Properties of Ecoflex-30 Silicone Rubber. **(A)** Photograph of the TA Instruments DMA 850 analyzer. **(B)** Square-shaped sample used for testing (dimensions: $18 \times 18 \times 6 \text{ mm}^3$). **(C, D)** Storage modulus **(C)** and loss factor **(D)** versus frequency at temperatures from 25°C to -30°C. **(E, F)** TTS-mastered curves (blue) at 25°C reference temperature, overlaid with direct DMA data (25°C, orange): storage modulus **(E)** and loss factor **(F)**.

The resulting TTS master curves extend the data up to 596 Hz (**Fig. S7E** for storage modulus and **Fig. S7F** for loss factor, shown in blue). The direct DMA frequency sweep (< 181 Hz) test results at 25°C (orange) and the extrapolated data (181-596 Hz) are presented together. The storage modulus and loss factor show a gradual, albeit fluctuating, increase at higher frequencies. Still, the

changes are minimal: for example, storage modulus rises from 152 kPa at 170 Hz to 164 kPa at 574 Hz, and loss factor increases from 0.191 to 0.208.

While direct DMA frequency sweeps remain the most straightforward method for assessing viscoelastic properties below 181 Hz, TTS provides evaluation for higher frequencies at the cost of increased experimental complexity and time. Notably, not all materials are amenable to TTS extrapolation due to deviations from thermos-rheological simplicity (9).

Cantilever Beam Resonance Method

As an alternative method to assess viscoelastic properties at discrete higher frequencies, we investigated the ASTM E756-05 standard (10) using a cantilever beam resonance setup. Rectangular beam samples (dimensions: $100 \times 6 \times 6 \text{ mm}^3$, **Fig. S8**) were clamped at one end and excited to measure resonance frequencies and damping. This yielded data only at specific resonance modes: 125.1 Hz (first mode), 190 Hz (second mode), and 255 Hz (third mode). The results are summarized in **Table S1** below, showing that the storage modulus and loss factor exhibit limited variation at elevated frequencies.



Fig. S8. Photograph of the test sample used for the cantilever beam resonance method.

Table S1. Viscoelastic Properties from Cantilever Beam Resonance Method

Frequency (Hz)	Storage modulus (kPa)	Loss modulus (kPa)	Loss factor
125.1	132	19	0.1415
190	136	21	0.1562
255	138	22	0.1581

5. Stability of Sound Absorption Performance

In this section, we investigated the stability of the FN-Helmholtz resonator's sound absorption performance across different environmental and operational conditions.

Long-term Stability

We measured the acoustic properties of the FN-Helmholtz resonator (the same sample shown in **Fig. 5F** in the main text) under ambient conditions (25 °C) at various time points: Day 1 (immediately after fabrication), Day 60 (60 days after fabrication), and Day 80 (80 days after fabrication). As illustrated in **Fig. S9**, the absorption coefficient, normalized acoustic resistance, and normalized acoustic reactance exhibit robust performance over time. The resonator sustains high absorption efficiency ($\alpha > 0.96$) across its operational bandwidth (231–338 Hz) even after 80 days. A minor shift in the absorption peaks toward higher frequencies is evident (e.g., the first peak shifts from 239 Hz to 243 Hz), which can be attributed to the natural aging of the silicone rubber. Importantly, this shift tends to stabilize after the initial period, as demonstrated by the nearly identical curves recorded on Day 60 and Day 80. For applications that demand exceptional long-term stability, strategies such as material modifications or process optimizations could be implemented to further mitigate these aging effects.

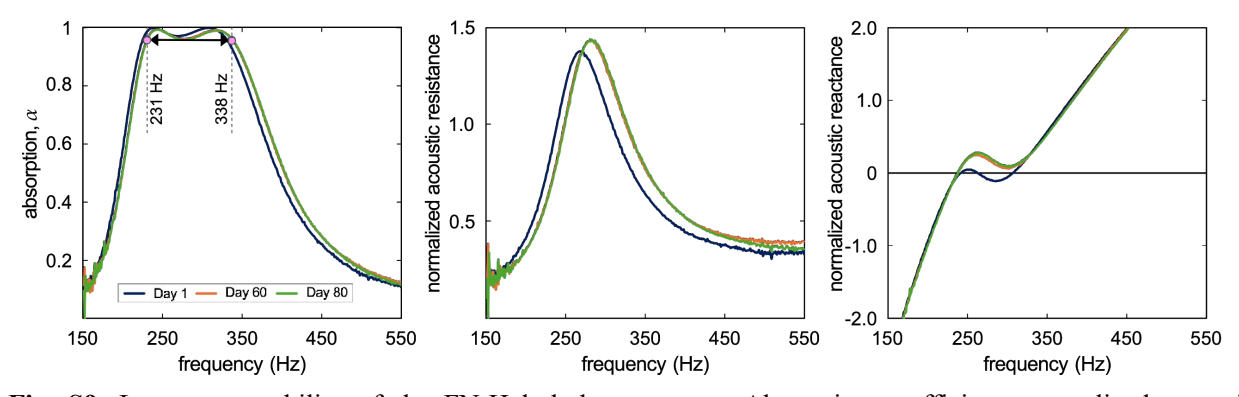


Fig. S9. Long-term stability of the FN-Helmholtz resonator. Absorption coefficient, normalized acoustic resistance, and acoustic reactance measured on Day 1, Day 60, and Day 80.

Temperature Effects on Sound Absorption Performance

Temperature variations may affect the viscoelastic properties of Ecoflex-30, potentially influencing the sound absorption performance of the FN-Helmholtz resonator. From the TTS raw data (**Figs. S7C and S7D**), decreasing temperature increases both storage modulus E and loss factor η (e.g., E rises from 152 kPa at 25°C to 169 kPa at -10°C; η rises from 0.19 to 0.22). To quantify the temperature effect, we conducted coupled acoustic-structural simulations in COMSOL Multiphysics using viscoelastic parameters at two representative temperature: 25°C and -10°C, with identical geometry to that in **Fig. 2A** (also shown in **Fig. S19**).

The simulated normal-incidence absorption spectra (**Fig. S10**) show minor shifts: the first peak frequency moves from 327 Hz at 25°C to 334 Hz at -10°C, while the overall broadband profile remains largely preserved. These results indicate that the FN-Helmholtz resonator maintains relatively stable broadband absorption performance across a wide temperature range.

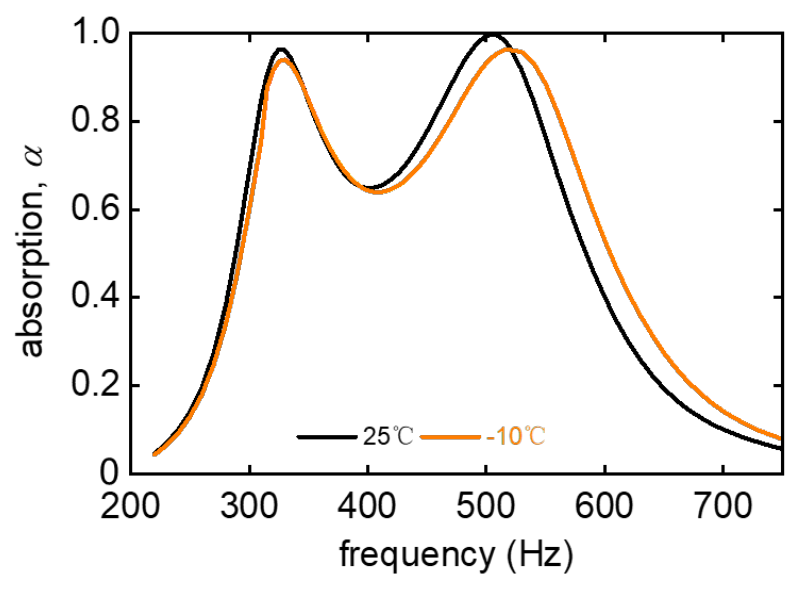


Fig. S10. Simulated sound absorption coefficients of the FN-Helmholtz resonator using viscoelastic parameters at 25°C (E = 152 kPa, η = 0.19; black curve) and -10°C (E = 169 kPa, η = 0.22; red curve).

Absorption Under Oblique Incidence

To extend the model's applicability to realistic scenarios involving non-normal incidence, we further consider oblique incidence at angle θ (measured from the normal to the surface). Assuming the surface is locally reacting, i.e., the acoustic impedance is independent of the angle of incidence, which is a valid approximation for resonant absorbers (11), the absorption coefficient $\alpha(\theta)$ is calculated by modifying the formula (Eq. 41) to account for the effective impedance projection along the direction of propagation:

$$\alpha(\theta) = 1 - \left| \frac{Z_e S \cos \theta - \rho_0 c_0}{Z_e S \cos \theta + \rho_0 c_0} \right|^2$$
 [63]

Using the full recursive model, we calculated the absorption spectra for representative incidence angles of 0°, 30°, and 60°. The calculations utilized geometric and material parameters identical to that in **Fig. S20**. As shown in **Fig. S11**, the absorption spectra vary with incidence angle, exhibiting differences across frequency bands. For instance, a reduction in absorption in the first peak at higher angles, accompanied by an increase in mid-frequency regions. These variations arise from changes in impedance matching between the absorber and the incident wave as a function of angle.

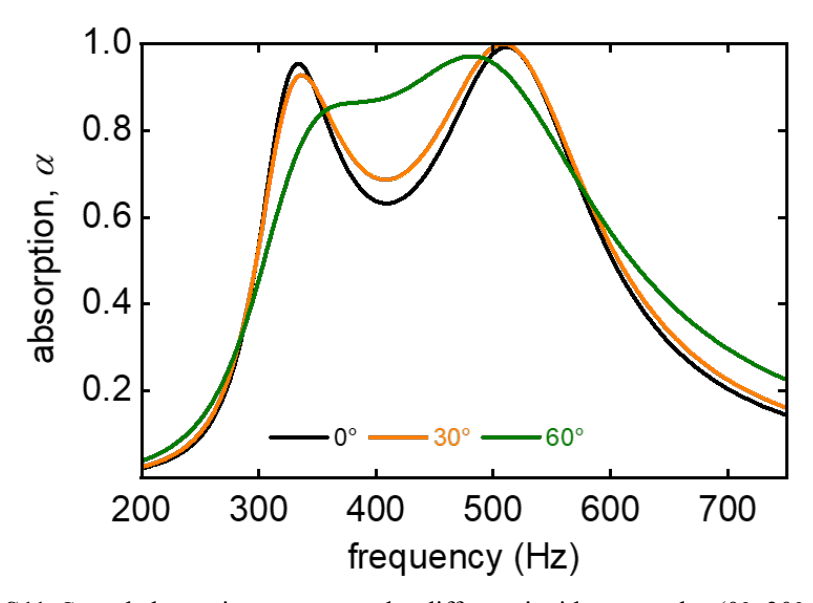


Fig. S11. Sound absorption spectra under different incidence angles (0°, 30°, 60°).

Absorption Under High Sound Pressure

To evaluate potential influences of material nonlinearity at elevated incident sound levels, the normal-incidence sound absorption coefficient of the FN-Helmholtz resonator (configuration as shown in **Fig. 2A**) was measured under white-noise excitation at various source levels: 90 dB (0.632 Pa), 100 dB (2 Pa), 110 dB (6.32 Pa), 120 dB (20 Pa), and 129 dB (56.2 Pa, the maximum output achievable by the impedance tube speaker), with the experimental setup shown in **Fig. S14**. The measured absorption curves are shown in **Fig. S12**.

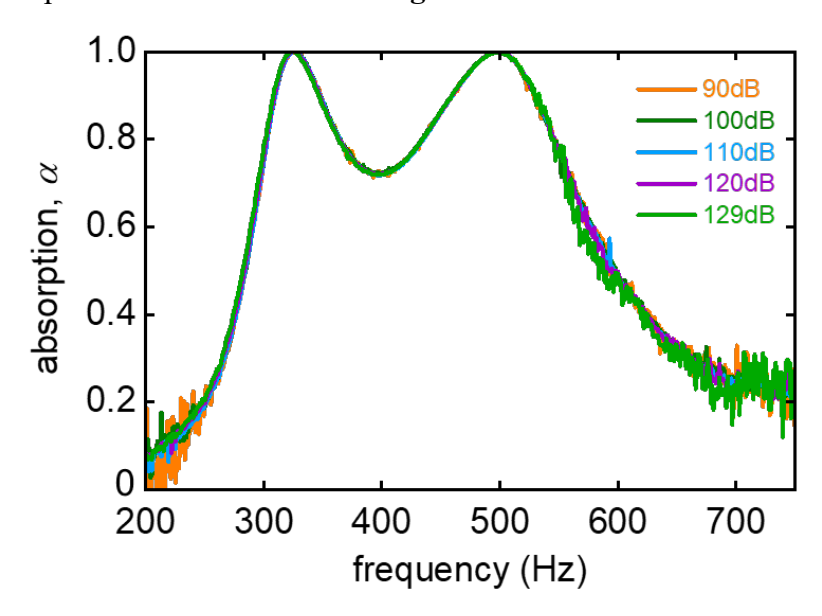


Fig. S12. Sound absorption spectra under various incident sound pressure levels.

All curves are nearly identical across this range of incident sound pressures, which indicates that the absorber operates linearly even at high excitation levels. We note that the curve at 90 dB appears slightly less smooth, which is attributed to a lower signal-to-noise ratio at this pressure level. Similarly, minor fluctuations are observed at high frequencies under 129 dB excitation, likely due to distortion or limitations of the acoustic source at its maximum output.

To quantitatively assess structural linearity, we performed finite element simulations in COMSOL Multiphysics (detailed in **Fig. S19**) to extract the maximum radial displacement and principal strain of the soft cylindrical shell under these incident sound pressures. The results are summarized in **Table S2** below:

Table S2. Simulated maximal displacement and strain of the soft shell under different sound pressure.

Sound pressure (Pa)	dB	Maximal displacement (mm)	Maximal strain
0.632	90	0.0005	0.016%
2	100	0.0017	0.051%
6.32	110	0.0052	0.162%
20	120	0.0165	0.511%
56.2	129	0.0464	1.440%

Even at the highest excitation level of 129 dB (56.2 Pa), the principal strain is only 1.44%. These values are well within the linear elastic regime of Ecoflex-30 silicone rubber, which has been reported to exhibit linear stress-strain behavior up to approximately 10% strain (12). Therefore, we conclude that the structural response of the soft shell is expected to remain linear at significantly high sound pressure levels, such as 129 dB. These results support the validity of the linear model used in our study. Potential acoustic nonlinearities in the air medium at even higher sound pressures were not explored in this study.

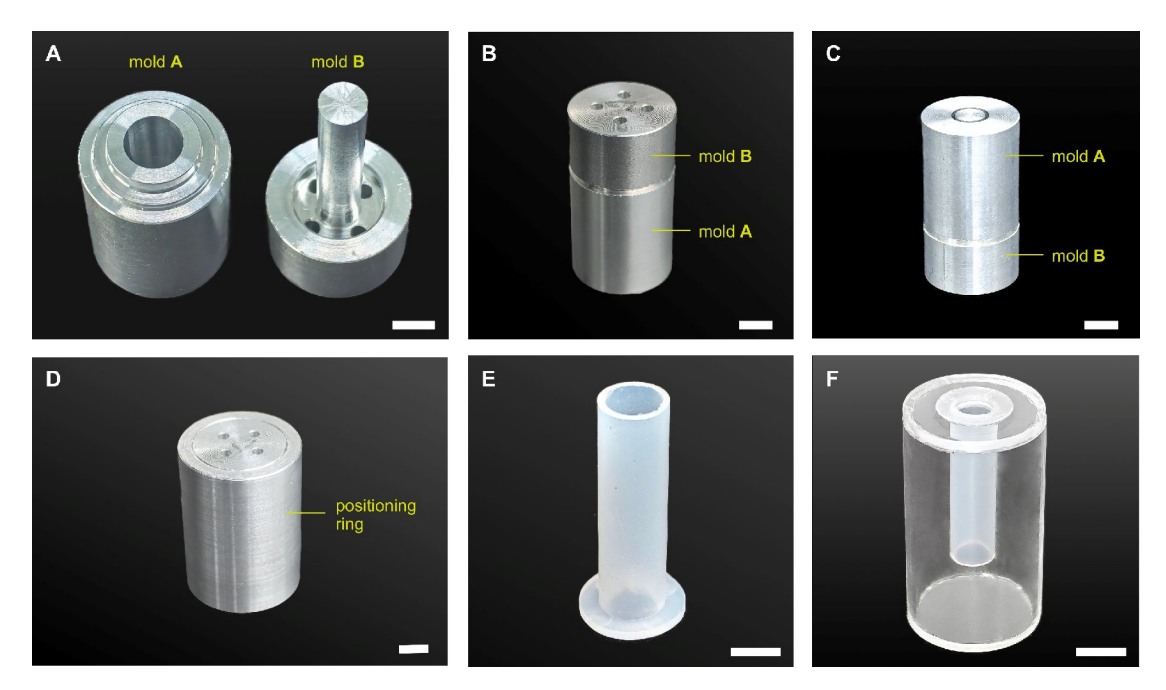


Fig. S13. Fabrication process of the FN-Helmholtz resonator. (A) CNC-machined aluminum alloy molds used for silicone casting, labeled as Mold A (left) and Mold B (right). Mold A contains a larger cylindrical cavity (inner diameter: 10 mm) with a sealed bottom (taped), while Mold B includes a central cylindrical pillar (diameter: 8 mm) and four peripheral through-holes for excess silicone precursor drainage. Mold A and Mold B have the same outer diameter. (B) Silicone precursor was injected into Mold A, and Mold B was inserted into the cylindrical cavity. The taped bottom prevented precursor leakage from the bottom. This created an annular gap filled with silicone precursor. Excess precursor drained through the four peripheral through-holes of Mold B. (C) Inverted view of the assembled molds, clearly showing the annual gap formed between the molds. (D) A positioning ring was nested around the outer surfaces of both molds to ensure accurate coaxial alignment throughout the mold length. (E) After 4 hours of curing, the molds were disassembled, and the silicone shell was demolded and trimmed to its final dimensions, with deviations below 0.05 mm from the mold design. (F) Final assembly of the FN-Helmholtz resonator, with the flexible shell integrated into the outer structure. For illustration, the outer shell is rendered as transparent acrylic; the actual test sample used opaque 3D-printed resin shell. Note: white scale bar = 10 mm in all panels.

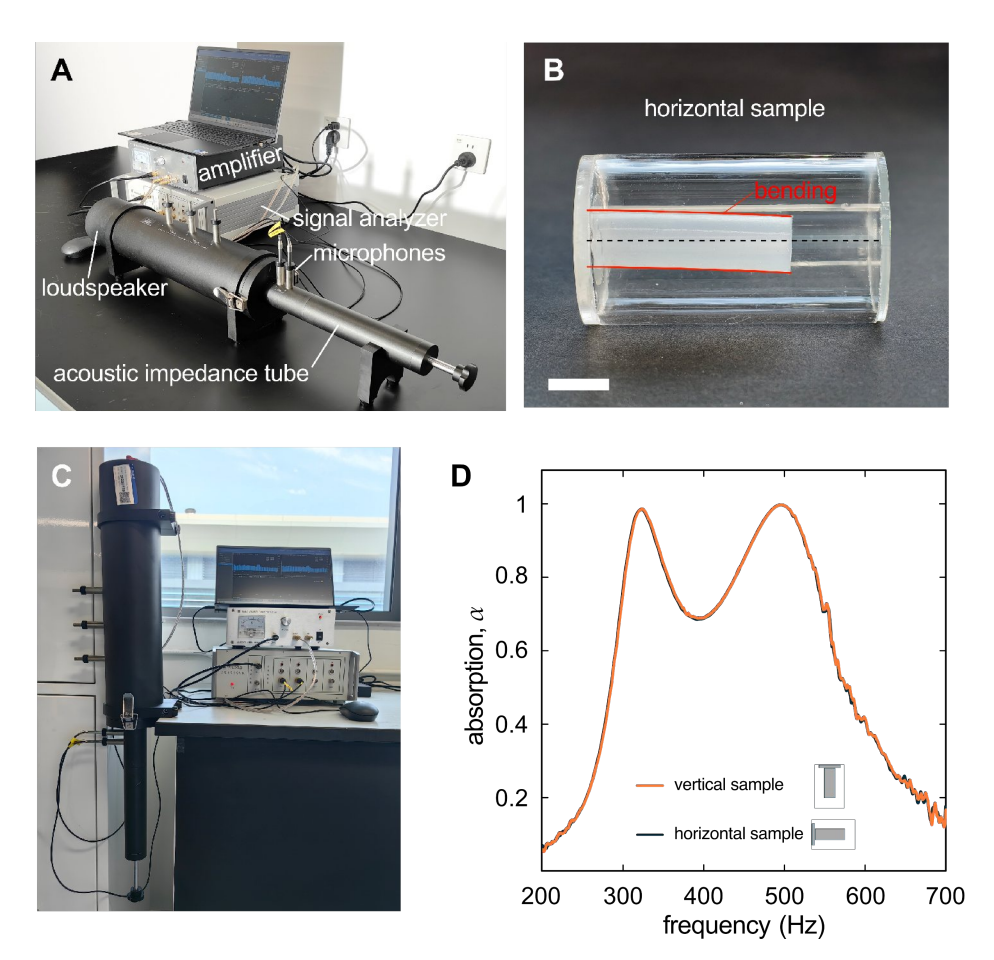


Fig. S14. Experimental setup for sound absorption measurements and assessment of sample orientation effects. (A) Photograph of the horizontally oriented acoustic impedance tube (AWA6290T, Hangzhou Aihua Instruments Co., Ltd.) with an inner diameter of $D=29\,$ mm. Measurements are conducted according to ISO 10534-2, utilizing broadband white noise excitation (50–6300 Hz, 110 dB SPL) and capturing acoustic signals with two microphones. Sound absorption coefficients were calculated using the transfer function method. (B) Photograph showing slight gravitational sagging of the flexible cylindrical shell due to its low stiffness in the horizontal position (white scale bar = 10 mm). (C) Photograph of the vertical setup, eliminating gravitational sagging. (D) Comparison of sound absorption coefficients for horizontal and vertical orientations, showing nearly identical results and confirming that sagging has negligible influence on acoustic performance under the tested sample conditions. The sample was made from Ecoflex-30 (Young's modulus $\approx 90\,\text{kPa}$; see Fig. 2B).

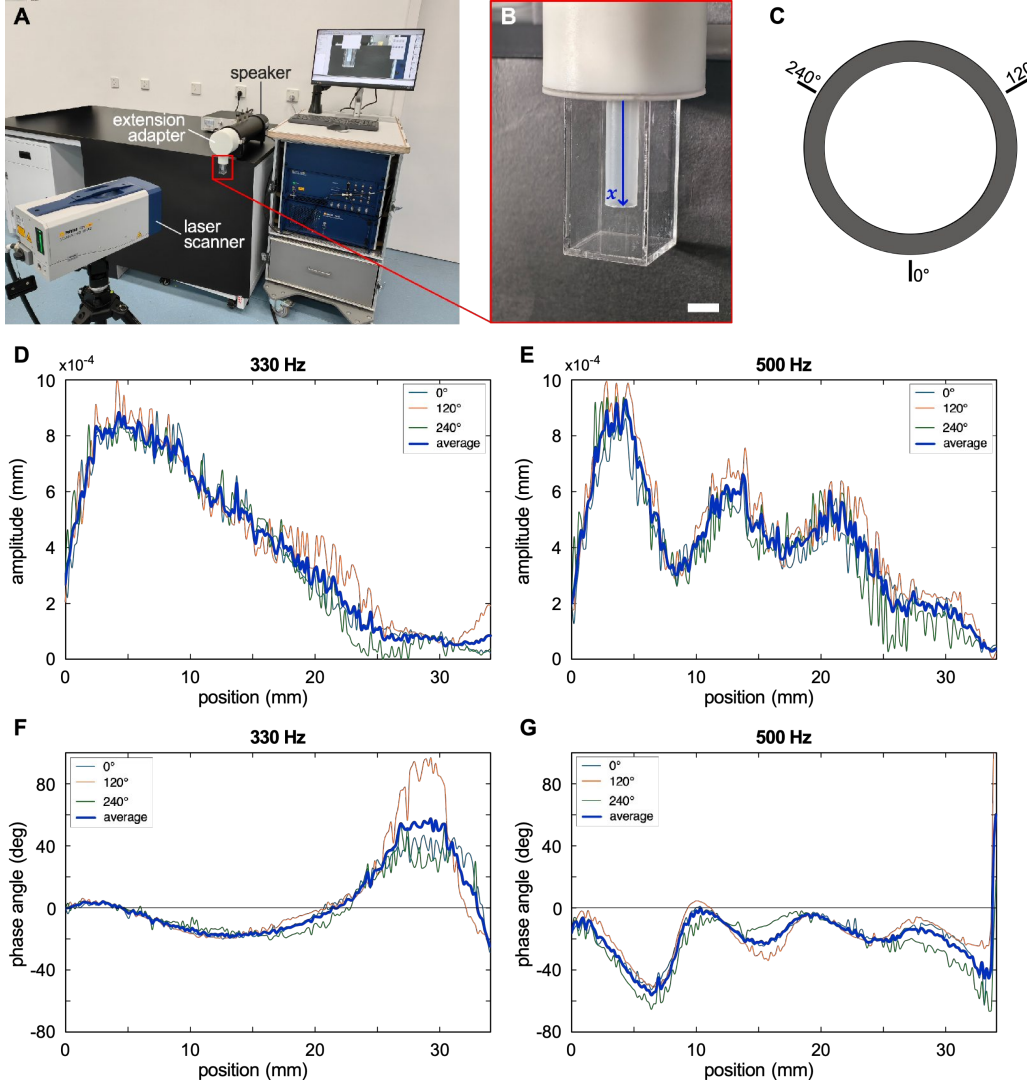


Fig. S15. Experimental setup and results for vibrational displacement of the silicone rubber cylindrical shell. (A) Photograph of the measurement setup, including a Polytec PSV-500 laser Doppler vibrometer, an acoustic impedance tube with a speaker as the sound source, and the tested sample mounted via a 3D-printed extension adapter. (B) Sample enclosed in a transparent acrylic shell designed for unobstructed laser access, with a rectangular cavity to minimize laser reflection artifacts. The internal volume of the rectangular cavity matches that of the cylindrical cavity in Fig. 2A. One end of the sample is designed to rotate to fixed angular positions, enabling scanning along different axial lines. Blue line indicates scanning axial scanning paths, with a spatial resolution of 0.2 mm. The true clamped end (l = 0 mm) is obscured by the fixture. Scanning starts at l = 2.5 mm (corresponding to x = 0) and ends at l = 36.5 mm (x = 34 mm), covering a distance of 34 mm axially. (C) Schematic showing the three circumferential positions (0°, 120°, and 240°) of the scanning lines. (D, E) Measured displacement amplitudes under (D) 330 Hz and (E) 500 Hz acoustic excitation along the three scanning lines. Blue curve shows the averaged amplitude profile. (F, G) Measured phase distributions of radial displacement at (F) 330 Hz and (G) 500 Hz across the three lines, referenced to the speaker input signal and normalized to zero phase at the scanning start point (x = 0). Blue curve shows the average phase profile.

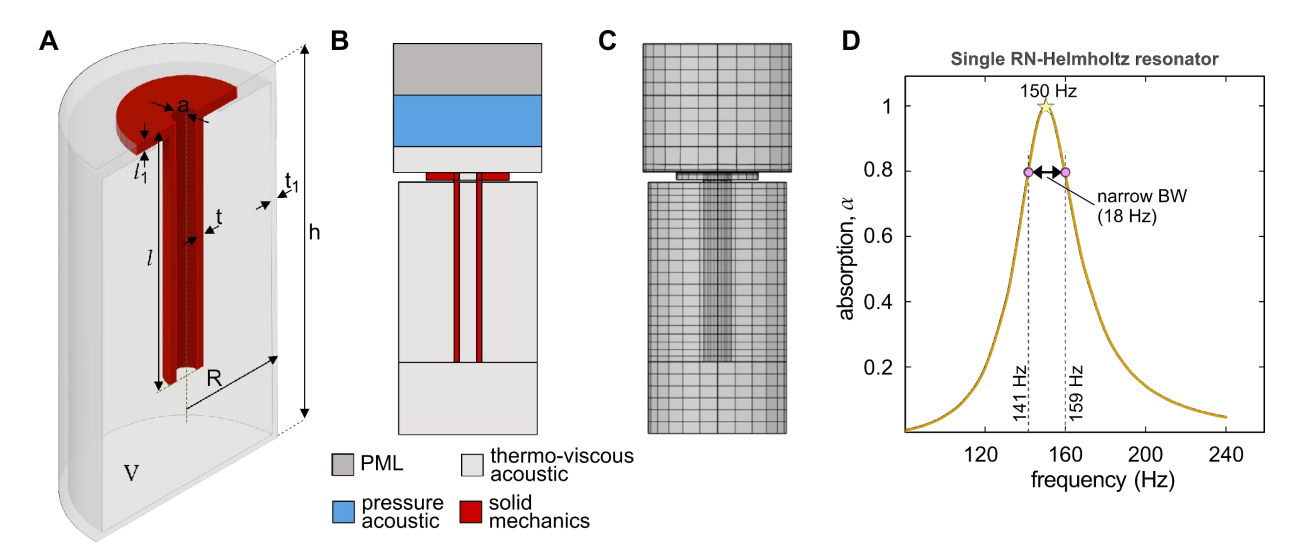


Fig. S16. Structural and simulation details of the RN-Helmholtz resonator model corresponding to Fig. 1A. (A) Cross-sectional schematic of the resonator. The cylindrical neck has a radius of a = 1.7 mm, wall thickness t = 1 mm, and length l = 37 mm, with a 1.5 mm segment (l_1) anchored to the outer shell. The cavity is enclosed by an outer cylindrical shell with radius R = 14.5 mm, thickness $t_1 = 1$ mm, and total height h = 52 mm. Both the cylinder neck and outer shell are modeled with a Young's modulus of E = 2,650 MPa, Poisson's ratio v = 0.4, density $\rho_3 = 1,120$ kg/m³, and loss factor $\eta = 0.01$. (B) Physical domain assignment used in the coupled acoustic–structure simulation in COMSOL Multiphysics. PML stands for perfectly matched layer. (C) Finite element mesh of the RN-Helmholtz resonator model. The domain is discretized using hexahedral elements, with locally refined boundary layers in the thermo-viscous acoustics region. (D) Simulated sound absorption coefficient. The RN-Helmholtz resonator exhibits a narrow absorption peak of 0.999 at 150 Hz, with an effective bandwidth ($\alpha > 0.8$) spanning only 18 Hz, from 141 to 159 Hz.

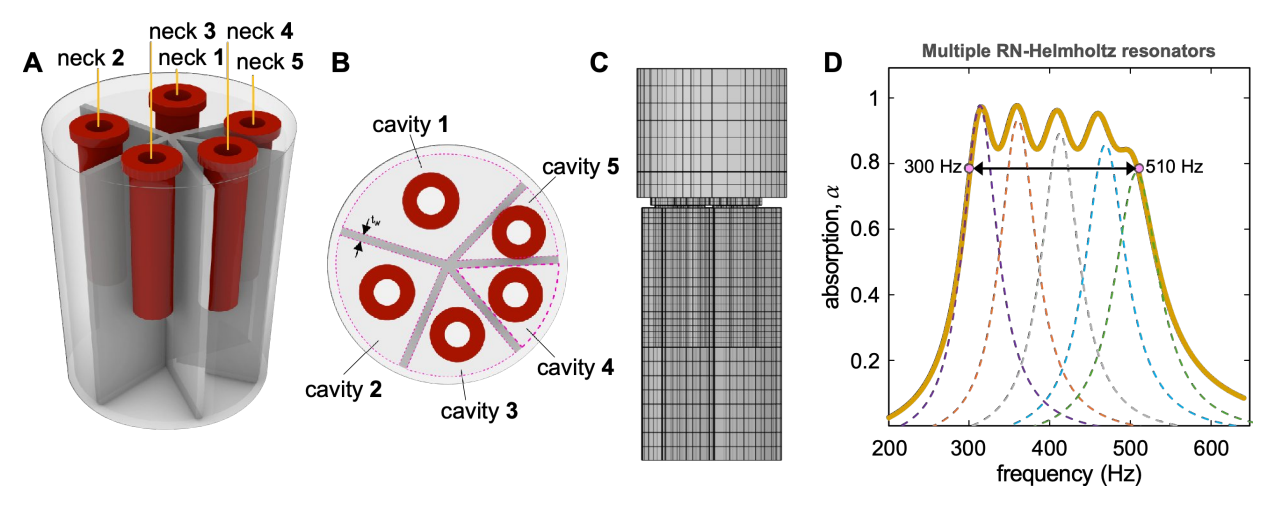


Fig. S17. Structural and simulation details of the Multiple RN-Helmholtz resonators model corresponding to Fig. 1E. **(A)** Schematic of the absorber integrating five resonators. The sample has a total height h = 52 mm and outer radius R = 14.5 mm. Each resonator contains a rigid neck of equal length (l = 29 mm) and wall thickness (t = 1 mm). The inner radii of the different tubes are: 3.35 mm for neck 1, 3.2 mm for neck 2, 3.1 mm for necks 3 and 4, and 2.95 mm for neck 5. Material properties are identical to those in Fig. S16. **(B)** Top view schematic of the resonators. The thickness of the partition walls between cavities is $t_w = 1$ mm. All cavities have the same height of 49 mm (excluding 3 mm top and bottom plates), but vary in cross-sectional area: 171 mm² (Cavity 1), 120.6 mm² (Cavity 2), 88 mm² (Cavity 3), 70.6 mm² (Cavity 4), and 56.2 mm² (Cavity 5). **(C)** Finite element mesh in COMSOL Multiphysics using hexahedral elements, with refined thermos-viscous boundary layers. **(D)** Simulated sound absorption coefficient of the coupled system shows broadband absorption (300-510 Hz, α > 0.8) with peaks at 315 Hz (0.971), 360 Hz (0.975), 410 Hz (0.960), 460 Hz (0.952), and 495 Hz (0.841). For comparison, the absorption spectra for individual resonators are also shown: Unit 1 (purple dashed line, 313 Hz peak, 0.976), Unit 2 (orange, 359 Hz, 0.932), Unit 3 (gray, 412 Hz, 0.890), Unit 4 (blue, 368 Hz, 0.856), and Unit 5 (green, 508 Hz, 0.769).

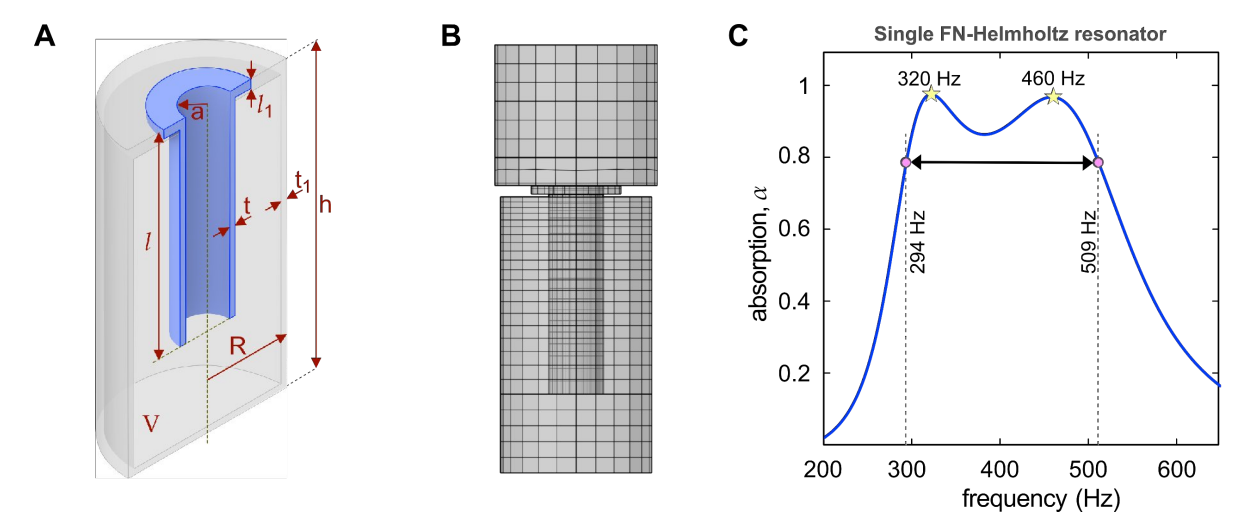


Fig. S18. Structural and simulation details of the FN-Helmholtz resonator model corresponding to Fig. 1F. (A) Cross-sectional schematic of the resonator. The design features a flexible cylindrical neck with radius a=3.87 mm, wall thickness t=1 mm, and length l=37 mm, with a 1.5 mm segment (l_1) anchored to the outer shell. The outer shell has a radius R=14.5 mm, thickness $t_1=1$ mm, and height h=52 mm. The flexible neck is modeled as a viscoelastic material with Young's modulus E=120 kPa, Poisson's ratio v=0.49, density $\rho_s=1,120$ kg/m³, and loss factor $\eta=0.4$. The material parameters of the outer shell are identical to those in Fig. S16. (B) Finite element mesh in COMSOL Multiphysics using hexahedral elements, with refined thermos-viscous boundary layers. (C) Simulated sound absorption coefficient of the FN-Helmholtz resonator shows two prominent absorption peaks at 320 Hz (0.974) and 460 Hz (0.967), resulting in a broadband absorption region where $\alpha > 0.8$ over a 215 Hz range (294–509 Hz), more than 10 times higher than that in the RN-Helmholtz resonator shown in Fig. S16D.

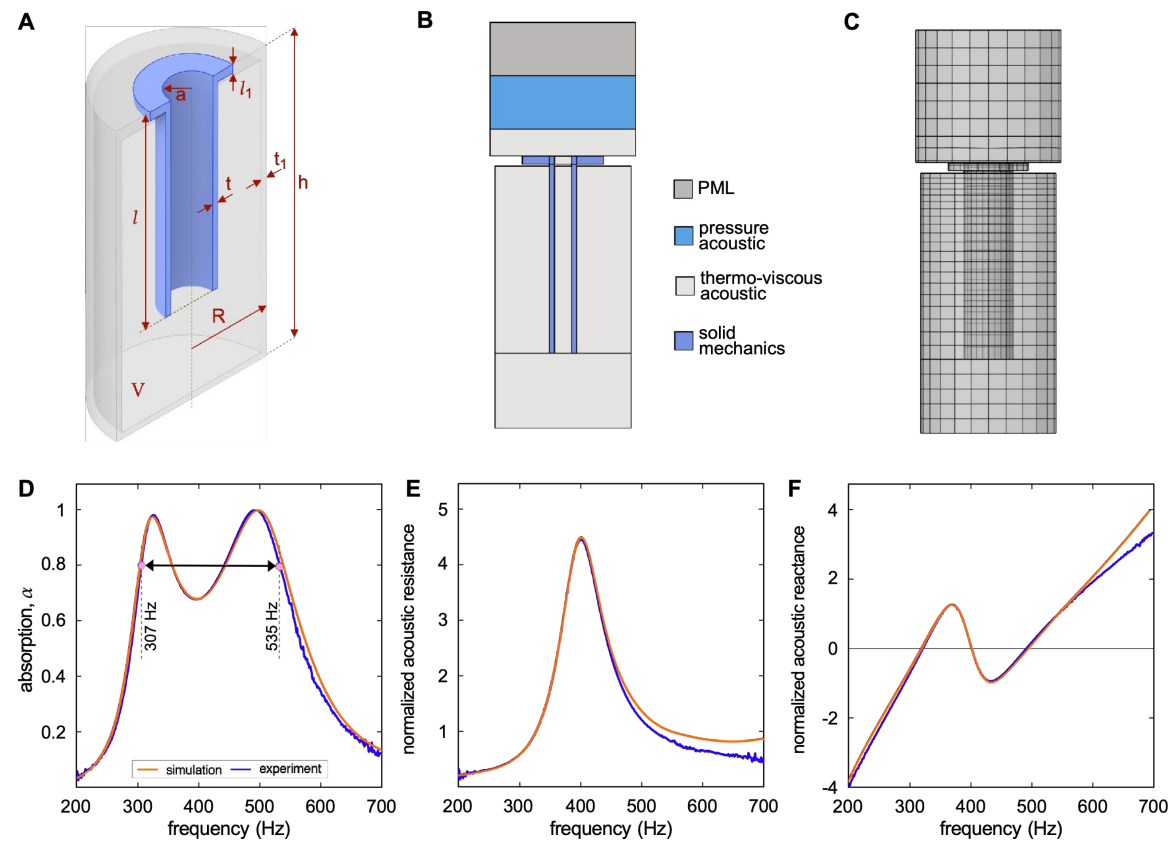


Fig. S19. Simulation model of the FN-Helmholtz resonator corresponding to Fig. 2A and comparison between simulation and experimental results. (A) Cross-sectional schematic of the resonator. The flexible cylindrical neck has a radius a=4 mm, wall thickness t=1 mm, and length l=36.5 mm, with a segment ($l_1=1.5$ mm) anchored to the outer shell. The outer shell has a radius R=14.5 mm, wall thickness $t_1=0.6$ mm, and total height h=51.5 mm. The neck material is modeled with Young's modulus E=148.5 kPa, Poisson's ratio v=0.49, density $\rho_s=1,070$ kg/m³, and loss factor $\eta=0.2$. (B) Physical domain assignment used in the coupled acoustic–structure simulation in COMSOL Multiphysics. A background pressure field of 1 Pa is applied in the pressure acoustic domain as the sound source. PML stands for perfectly matched layer. (C) Finite element mesh in COMSOL Multiphysics using hexahedral elements, with refined thermos-viscous boundary layers. (D-F) Comparison of simulation and experimental results: (D) sound absorption coefficient, (E) normalized acoustic resistance, and (F) normalized acoustic reactance, all demonstrating close to excellent agreement.

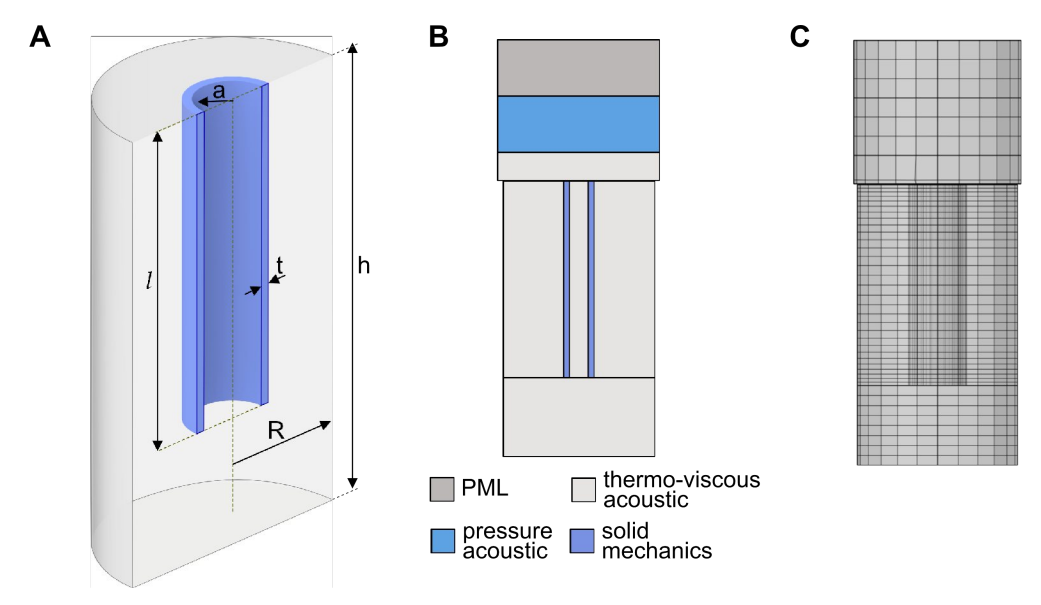


Fig. S20. Simulation model (corresponding to Fig. 3) for validation against analytical solution. (A) Cross-sectional schematic of the model geometry. The cavity has a height h = 48.8 mm and radius R = 13.9 mm. The cylindrical shell has a radius a = 4 mm, thickness t = 1 mm, and length l = 35 mm. The cylindrical shell material is modeled with a Young's modulus E = 148.5 kPa, Poisson's ratio v = 0.49, density $\rho_s = 1,070$ kg/m³, and loss factor $\eta = 0.2$. (B) Physical domain assignment in the COMSOL Multiphysics acoustic-structural simulation model. (C) Finite element mesh in COMSOL Multiphysics using hexahedral elements, with refined thermosviscous boundary layers.

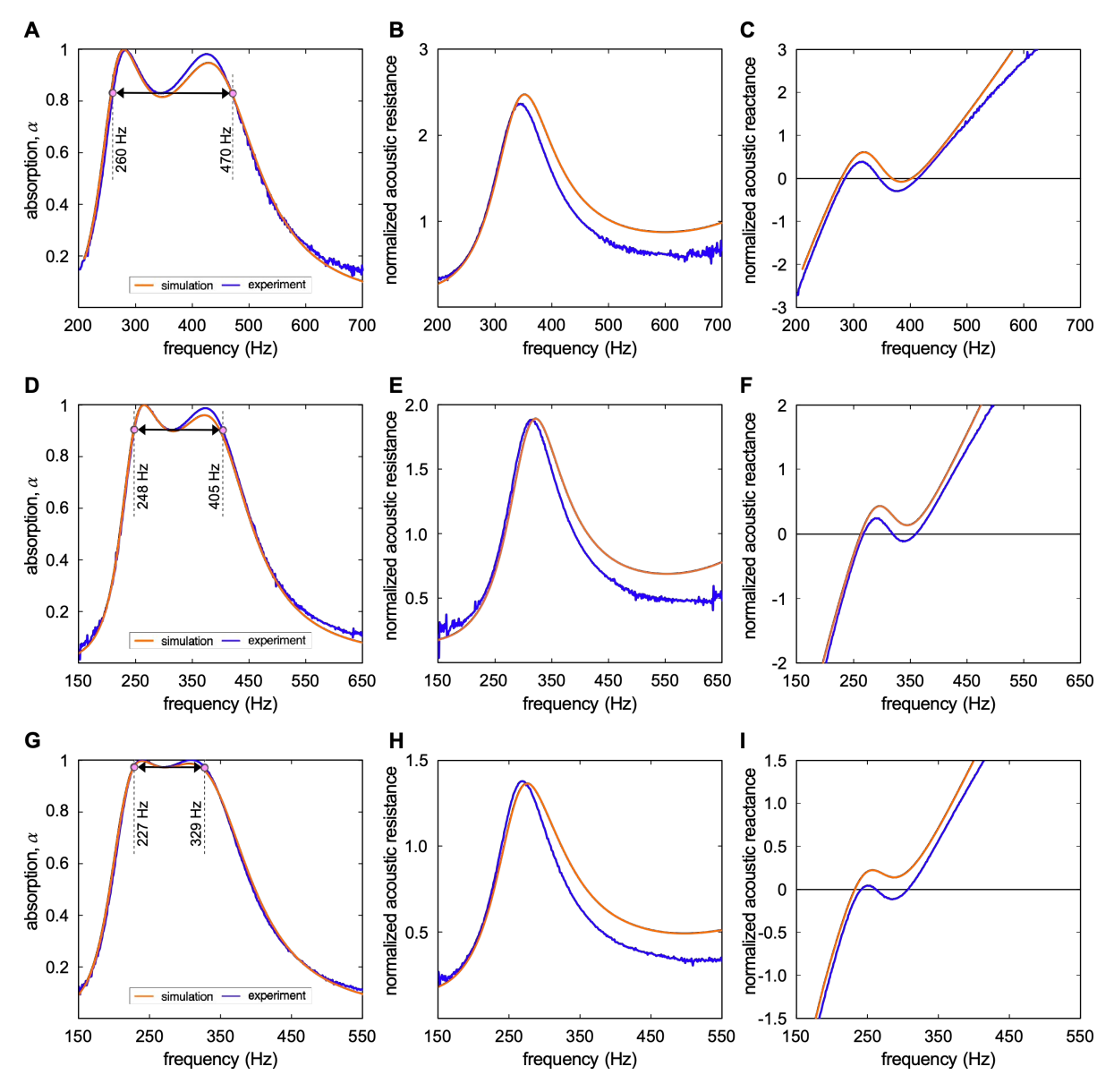


Fig. S21. Experimentally measured and simulated acoustic properties for three resonator sets. **(A-C)** Set 1 (Ecoflex-20; a = 4 mm, l = 41.5 mm, t = 1 mm, h = 63 mm), showing (A) absorption coefficient, (B) normalized acoustic resistance, and (C) normalized acoustic reactance. **(D-F)** Set 2 (Ecoflex-0020 + W; a = 4 mm, l = 41.5 mm, t = 1 mm, t = 1

SI References

- [1] I. B. Crandall, Theory of vibrating systems and sound (D. Van Nostrand Company, 1926).
- [2] P. M. Morse, K. U. Ingard, Theoretical acoustics (Princeton University Press, 1986).
- [3] U. Ingard, On the theory and design of acoustic resonators. J. Acoust. Soc. Am. 25, 1037–1061 (1953).
- [4] S. Timoshenko, S. Woinowsky-Krieger, Theory of Plates and Shells. 2nd ed. (McGraw-Hill, 1989).
- [5] G. Du, Z. Zhu, X. Gong, Fundamentals of Acoustics. 3rd ed. (Nanjing University Press, 2012).
- [6] W. B. Jones, W. J. Thron, Continued Fractions: Analytic Theory and Applications. Encyclopedia of Mathematics and its Applications (Cambridge University Press, 1980).
- [7] Y. Ding, A. P. Sokolov, Breakdown of time-temperature superposition principle and universality of chain dynamics in polymers. Macromolecules 39, 3322–3326 (2006).
- [8] M. L. Williams, R. F. Landel, J. D. Ferry, The temperature dependence of relaxation mechanisms in amorphous polymers and other glass-forming liquids. J. Am. Chem. Soc. 77, 3701–3707 (1955).
- [9] D. J. Plazek, The temperature dependence of the viscoelastic softening and terminal zones of linear poly(vinyl acetate). J. Polym. Sci. Polym. Phys. Ed. 20, 729–742 (1982).
- [10] ASTM International, ASTM E756-05: Standard test method for measuring vibration-damping properties of materials (ASTM International, West Conshohocken, PA, 2005).
- [11] J. Allard, N. Atalla, Propagation of Sound in Porous Media: Modelling Sound Absorbing Materials, 2nd ed. (Wiley, 2009).
- [12] C. Romano, et al., Tunable soft pressure sensors based on magnetic coupling mediated by hyperelastic materials. Soft Sci. 4, 3 (2024).